ACS Photonics

Article

Cite This: ACS Photonics XXXX, XXX, XXX−XXX

Nanoparticle-Assisted STED Nanoscopy with Gold Nanospheres

Nicolai T. Urban,[†,∥] Matthew R. Foreman,[‡] Stefan W. Hell,[†] and Yonatan Sivan*[,§]

[†]Department of NanoBiophotonics, Max Planck Institute for Biophysical Chemistry, 37077 Göttingen, Germany

[‡]Blackett Laboratory, Department of Physics, Imperial College London, London SW7 2AZ, United Kingdom

[§]Unit of Electro-optics Engineering, Faculty of Engineering Sciences, Ben-Gurion University of the Negev, P.O. Box 653, Be'er Sheva 8410501, Israel

ABSTRACT: We demonstrate stimulated emission depletion (STED) microscopy with 20 nm gold nanospheres coated by fluorescently doped silica. We demonstrate significantly improved spatial resolution down to 75 nm, which is the first time that hybrid NPs are used in STED imaging beyond the diffraction limit of confocal microscopy. Unlike previous demonstrations of super-resolution with metal nanoparticles with different techniques, this 3.3-fold resolution improvement was limited only by the particle size. The STED intensity required for this is almost twice lower than for conventional STED based on dye alone, and we observe no melting or displacement of the NPs at the utilized intensities. Moreover, we show that the nanoparticles can be imaged in an aqueous environment, demonstrating the relevance to bioimaging. Finally, we also show, for the first time in this context, an up to 3-fold reduction in the rate of photobleaching compared to standard dye-based STED, thus enabling sustainably brighter images.

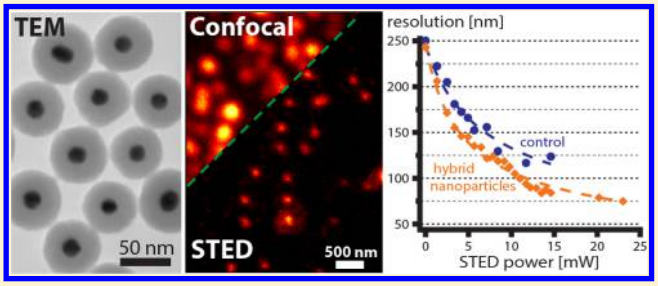

KEYWORDS: *STED nanoscopy, super-resolution, fluorescence microscopy, plasmonics, nanotechnology, nanoparticles*

In recent years, there has been a rapid growth in the use of nanoparticles (NPs) for various applications. Metal nanoparticles,[1] in particular, are finding applications in light concentration and harvesting in solar cell applications,[2] sanitation,[3,4] sensing,[5] surface-enhanced Raman scattering,[6] triggering chemical reactions,[7] super-resolution microscopy,[8−10] and many others. In the context of biological applications, they are being used for drug delivery[11] and cancer therapy,[12] for biodiagnostics,[13] as nanoscale sources of heat and acoustic waves,[14,15] as contrast agents in phase interferometry,[16] and more.

Frequently, a metal NP or nanostructure is combined with a standard fluorescent label used in bioimaging so as to create a hybrid fluorescent label, with the goal of exploiting the strong fields occurring at the localized plasmon resonance (LPR)[1] to boost the performance of the label. Specifically, such labels have been used for controlling the fluorescence lifetime and yield (also known as fluorescence engineering) and as a means to mitigate photobleaching[17−20] and increase signal brightness.[21]

Recently, Sivan et al. proposed and demonstrated how such hybrid fluorescent labels can be used within the context of the super-resolution imaging technique called stimulated emission depletion (STED) nanoscopy.[22] Specifically, it was shown theoretically[23−26] that the near-field enhancement occurring at the LPR can be exploited to reduce the required intensity of the STED beam and to reduce the bleaching rates through the shortening of the lifetime of the excited singlet level; this technique is referred to as nanoparticle-assisted STED nanoscopy (NP-STED). The lowering of the STED intensity was demonstrated experimentally using 150 nm gold shell NPs with a STED beam at $\lambda_{STED} \approx 780$ nm.[27] However, the resolution level demonstrated in that work was limited to only a slight improvement with respect to the diffraction limit. A more recent study[28] demonstrated a similar level of resolution even though the NPs used were much smaller. In addition, a reduction of the bleaching rate has to date not been demonstrated in this context.

Clearly, realistic applications of NP-STED in bioimaging may ensue only once substantial resolution improvement below the diffraction limit is demonstrated with an NP-STED label. In particular, more than a 2-fold improvement with respect to the diffraction limit is necessary in order to outperform alternative approaches such as structured illumination microscopy.[29] This can be done with NP-STED labels that are small enough to be able to benefit from the enhanced spatial resolution, to enjoy the maximum field enhancement levels, and to minimize interference with the biological system. NP-STED would also benefit from extending the range of operating wavelengths and functions of the hybrid fluorescent labels.

In this article, we provide a step toward fulfilling these goals. Specifically, a 3.3-fold improvement of resolution with respect to the diffraction limit of confocal microscopy is achieved, reaching resolutions of ∼75 nm, while requiring ∼2 times lower input intensity than needed for the standard dye. This is achieved in an aqueous environment and with no damage to

Special Issue: Recent Developments and Applications of Plasmonics

Received: July 26, 2017
Published: November 15, 2017

DOI: 10.1021/acsphotonics.7b00833
ACS Photonics XXXX, XXX, XXX−XXX

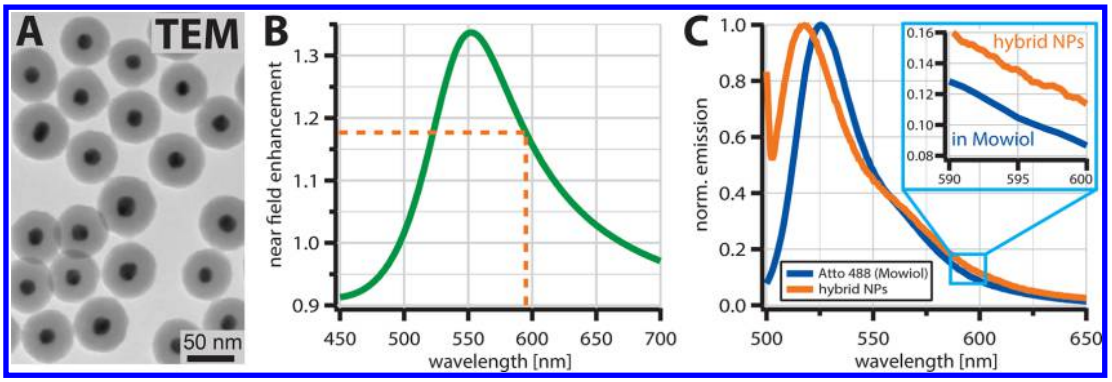

Figure 1. Hybrid nanoparticles. (A) TEM image of the synthesized NPs, with 20 nm Au cores surrounded by 20 nm thick, dye-doped glass shells. (B) Theoretical spatially and orientationally averaged near-field intensity enhancement for the hybrid NPs immersed in water; highlighted is the enhancement value of 1.18 at the used STED wavelength (595 nm). (C) Experimental normalized emission spectra for both hybrid NPs and free Atto 488 in Mowiol; note the difference at 595 nm of 0.14 (NPs) and 0.10 (Mowiol).

the NPs, thus demonstrating the relevance to imaging of biological samples. We also demonstrate, for the first time in this context, a reduced photobleaching rate induced by the presence of the metal NPs. Finally, we compare the performance of our NPs to those reported previously[27,28] and discuss the route toward realizing the full potential of NP-STED.[23] We also argue that even the existing implementation of NP-STED can be immediately combined with a wide range of imaging and treatment procedures utilizing metal NPs in a biological context.

PRINCIPLES OF NP-STED

The hybrid plasmonic-fluorescent labels used in this study consisted of 18.8 ± 1.9 nm diameter gold spheres coated with a 20.5 ± 1.1 nm glass shell doped with a standard green STED dye (Atto 488, which absorbs at ∼500 nm, emits at ∼525 nm, and has a lifetime in the nanosecond range). The fluorophores were uniformly and symmetrically distributed in the silica shell, thus avoiding issues associated with undesired shifts of the emitted signal.[30] The particles, shown in Figure 1A, synthesized by Nanocomposix Inc., are substantially smaller than the gold shells used before[27] and are substantially easier to fabricate (like the somewhat even smaller rods employed in ref 28) as compared to the thin gold nanoshells required for optimal NP-STED performance.[23,24] The STED intensity reduction due to the average near-field enhancement levels associated with this gold-core design is, however, substantially lower than those predicted for thin metal shells. The reason for this is that, unlike the rather uniform field experienced by dye *inside* a metal shell, the dye *around* a metal sphere experiences a field that decays as a function of the distance from the metal shell.

Indeed, Figure 1B shows the near-field enhancement (defined as Γ_I in ref 24 and taken relative to a homogeneous Mowiol environment; see below) that was calculated using the parameters indicated above and averaged over the volume of the dye-doped glass coating for NPs in an aqueous environment. Note that, in general, we will denote the enhancement ratio of an NP-enhanced quantity relative to the standard dye by Γ_j. It can be seen that at the local plasmon resonance, $\lambda_{LPR} \approx$ 553 nm, the (spatially) averaged near-field enhancement[31] is about ∼1.34. It was shown previously[24,25] that this value gives a reasonable estimate for the actual effective STED intensity reduction as calculated accurately with a doughnut-shaped illumination (as, for example, performed in the initial studies of NP-STED[23]). In our setup, we opted for a STED wavelength of λ_{STED} = 595 nm, which is standard for green dyes such as Atto 488, but is slightly detuned from the plasmon resonance. At this wavelength the average near-field enhancement is $\sim 1.18^{+0.12}_{-0.1}$, where the bounds account for size variations within the manufacturer tolerances.

Besides overlapping with the STED wavelength, the plasmon resonance overlaps partially with the emission line of the dye, giving rise to a shortening of the fluorescence lifetime.[1,32] In general, the decay rate enhancement depends strongly on position and the relative orientation of the emitter with respect to the metal surface. The cumulative signal emanating from a collection of such emitters typically exhibits a multiexponential decay pattern.[1,33] Frequently, however, the decay curve is approximated with low-order or even monoexponential decay curves.[1,34] In the latter case, one can define the decay rate enhancement, Γ_I, with respect to the free dye decay rate.[24] As long as the STED pulse duration is substantially shorter than the dye lifetime, there should be little influence on the STED efficiency of the nanoscope.[24,35,36] If, however, the STED pulse duration approaches the dye lifetime or even becomes longer, then the STED efficiency will notably decrease. The effects of this can be (partially) compensated by using time-gated detection, with the caveat that time-gating will result in somewhat lower signal brightness. Under such time-gated collection, we have shown theoretically that the averaged near-field enhancement Γ_I provides a good estimate of the STED intensity reduction that can be expected from the presence of the metal NP.[24,31] Additionally, the fluorescence signal will further decrease due to the reduction of the apparent quantum yield (quenching) originating from energy transfer to the metal, an effect enabled by the proximity of the fluorescent dye to the metal.

The lifetime shortening due to the NP has a positive effect as well, namely, an associated reduction of bleaching. Indeed, the shortened time the molecule spends in an excited state reduces the overall number of chemical reactions that may lead to photobleaching (such as absorption to an excited state or intersystem crossing to a triplet state[37−39]). This effect was described by Enderlein[40,41] and recently was demonstrated experimentally[18,19] on single fluorescent molecules, showing a 5-fold reduction of the spatially averaged bleaching rate. This value was found to be in good agreement with the theoretical prediction (for monochromatic and uniform excitation) of the total photon yield, being equal to the ratio of the emission and bleaching rates. A fuller analysis, accounting for the spatial

DOI: 10.1021/acsphotonics.7b00833
ACS Photonics XXXX, XXX, XXX−XXX

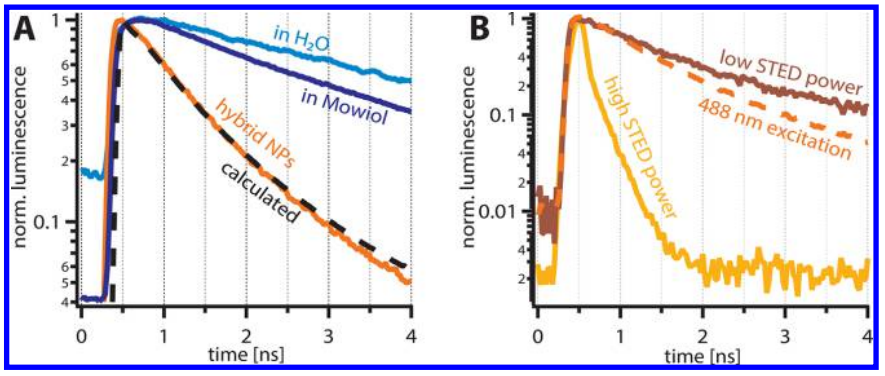

Figure 2. Fluorescence decay of Atto 488 under different circumstances. (A) Confocal measurements show that the lifetime of Atto 488 is shortened considerably (τ = 0.9 ns, orange) when within the hybrid nanospheres, as opposed to within an immunohistochemically labeled cell (τ = 2.8 ns, dark blue) or suspended in water (τ = 4.2 ns, light blue). The shortened lifetime within the NPs matches well with the theoretical model (τ = 0.95 ns, black dashed). (B) When illuminated only with the STED beam (dark red), the hybrid NPs emit fluorescence with similar decay characteristics to regular excitation (orange dashed). If the STED power is high enough (yellow), the fluorescence is surpassed by metal luminescence with a very short lifetime, in the range of the system response function.

variation of both the lifetime shortening and near-field enhancements,[20] has further shown theoretically and confirmed experimentally that the resulting aggregate bleaching behavior can exhibit a multiexponential behavior. An additional advantage associated with the decay rate enhancement is that it allows higher excitation powers to be used, since the saturation threshold increases.[21] All these effects naturally enable much brighter signals, thus compensating for the decrease of the quantum yield.

RESULTS

At first, we compared the fluorescence decay of the Atto 488 dye within the nanoparticle samples with measurements of free Atto 488 in water, as well as of Atto 488 used for immunohistochemically labeling fixated cells embedded in Mowiol. As can be seen in Figure 2A, under 488 nm excitation the measured lifetime of the dye contained within the nanoparticles was considerably shorter (τ = 0.9 ns) than when contained in fixated cells (τ = 2.8 ns) or when freely suspended in water (τ = 4.2 ns). The measured fluorescence decay within the NPs closely matched theoretical calculations of the lifetime shortening (τ = 0.95 ± 0.18 ns where bounds again account for possible size variation).

Besides the fluorescence, an additional source of luminescence became visible when illuminating the NPs with increasing STED power (Figure 2B). For simplicity, all stated laser powers correspond to the measured power in the back focal aperture of the objective lens ($P_{\mathrm{STED}}^{\mathrm{inc}}$). Using only the 595 nm STED beam as illumination, at low STED power (<10 mW) only a dim fluorescence signal could be detected originating from the NPs; it had a clear quadratic dependence on the incident intensity, hinting at a two-photon process. As the STED power was increased beyond 10 mW, the dim fluorescence was quickly overwhelmed by a growing, fast luminescence signal, the lifetime of which was measured to be virtually indistinguishable from the instrument response function, i.e., faster than ~200 ps (Figure 3A). The fast luminescence emanating from the metal NPs was clearly doughnut-shaped (Figure 3B), as was observed in previous studies.[27] Furthermore, this luminescence signal was orders of magnitude brighter than the reflected signal from a plane mirror sample at identical illumination powers (data not shown) and could be observed over a wide range of wavelengths (from blue to green) at similar count rates. The

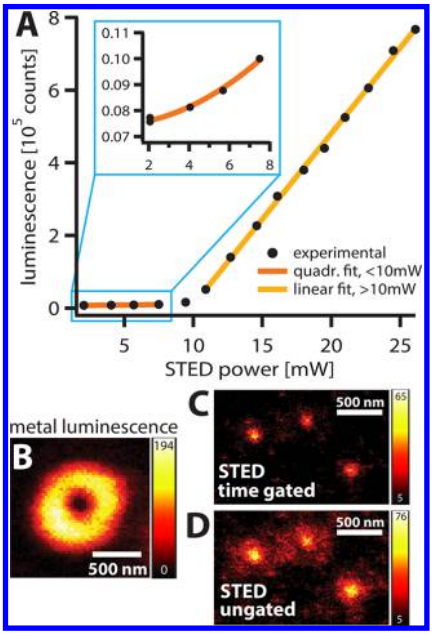

Figure 3. Metal luminescence from the NPs under intense STED illumination. (A) When illuminating the NPs with only 595 nm light < 10 mW, a weak fluorescence signal is visible (orange), which scales quadratically with the applied STED power. If the illumination intensity is increased above ~10 mW, then a second source of luminescence appears (yellow), which increases linearly in power and quickly drowns out the fluorescence. This metal luminescence displays a very short lifetime and a doughnut-shaped intensity profile (B). When recording proper STED images, the metal luminescence can be mostly discarded if the detection is time-gated (C), as opposed to using the entire detected signal (D).

power dependence of the fast luminescence at high illumination powers was linear (Figure 3A), suggesting a single-photon process. Due to the above, we can safely ascribe the unwanted luminescence at low powers to two-photon fluorophore excitation by the STED beam, a known feature of the Atto dye family, while the luminescence at higher powers clearly originates from the metal. Indeed, metal luminescence is known to be very fast and to have a rather wide bandwidth.[42,43] We do note, however, the difference with respect to the previous observation of metal luminescence in the context of NP-STED: previously,[27] using a STED wavelength of 780 nm, the

DOI: 10.1021/acsphotonics.7b00833
ACS Photonics XXXX, XXX, XXX−XXX

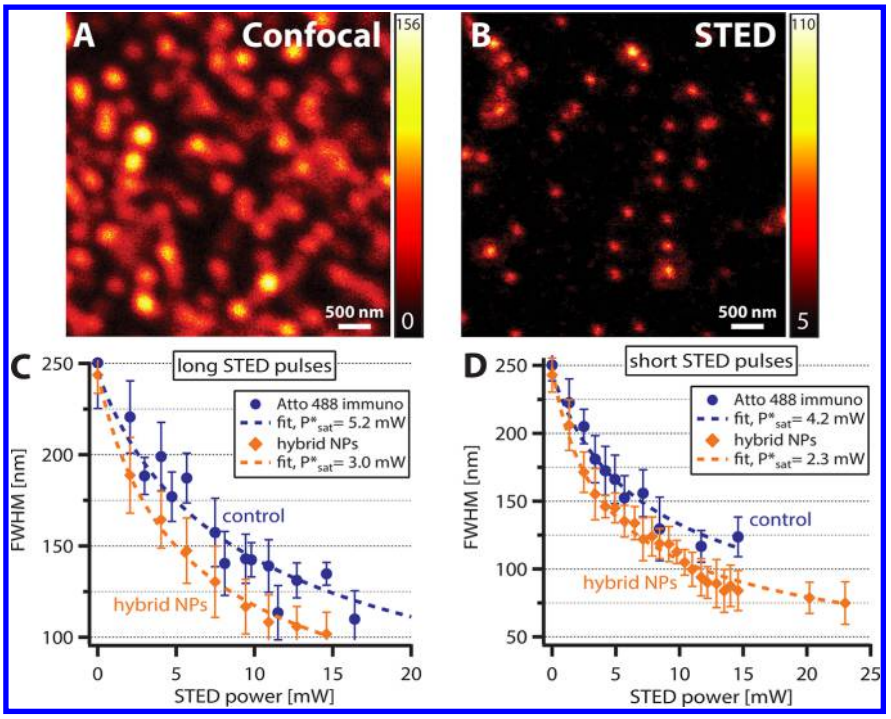

Figure 4. STED resolution enhancement for NP and control samples. Hybrid NPs recorded in (A) confocal and (B) STED mode (P^{inc}_{STED} = 10 mW). At identical STED powers, the hybrid NPs exhibited smaller fwhm's than the control samples. Displayed are averages ± standard deviation, for ≥25 samples. Data were fitted with an inverse square-root law; the resulting saturation powers P^{*}_{sat} are denoted in the figure. The ratio of saturation powers remained the same when measured using longer (200 ps, C) or shorter (50 ps, D) pulses, even though shorter STED pulses allowed higher absolute spatial resolutions of ∼75 nm (limited only by the NP size), in part due to a more efficient gating of the metal luminescence background.

luminescence seemed to scale with the square of the intensity, indicating two-photon absorption within the metal NP. For the much smaller NPs explored here, using a somewhat shorter wavelength of 595 nm, the luminescence seems to originate from single-photon absorption.

Due to the very short duration of the metal luminescence signal, it was readily eliminated using time-gated detection (Figure 3C). By discarding the first 450 ps of the recorded signal, the signal originating solely from the fluorophores could be analyzed without being obstructed by the luminescence from the gold cores (Figure 3D). As previously noted, time-gating also served to eliminate a possible loss of STED efficiency, as the lifetime within the NPs was shortened in regard to the duration of the STED pulse. At 595 nm illumination powers higher than ∼20 mW in the back focal aperture, however, the fast luminescence signal grew too strong to be ignored, as it began saturating the detector. Because the time-gating occurred after the detection (but before the acquisition), it could not prevent the saturation of the detector.

Next, we determined the achievable resolution of the hybrid NPs compared to the fixed-cell control samples for a given STED power P_{STED}; that is, we determined the different saturation intensities I_{sat} of the hybrid NP and the standard dye. We estimated the achievable resolution by measuring the average fwhm (full-width at half-maximum) of the imaged structures (beads or filaments) at different STED powers, using time-gated detection. For simplicity, we again use the measured incident STED power P^{inc}_{STED} in the back focal aperture of the objective lens as a reference value. The resolution increase over confocal imaging due to STED (see Figure 4A,B) follows an inverse square-root law, $d_{STED} \approx d_{conf}/\sqrt{1 + P^{inc}_{STED}/P^{*}_{sat}}$, where the effective saturation level is $P^{*}_{sat} \equiv P_{sat}/\Gamma_I$ and $P_{sat} \approx hc/[\lambda_{STED}\sigma_{em}(\lambda_{STED})T_{STED}]$. Note that this expression differs by a factor of $(k_{tot}T_{STED})^{-1}$ from the expression for the saturation intensity used, e.g., in molecular physics, laser systems etc.; see discussion in refs 25 and 44. (Here σ_{em}, λ_{STED}, and T_{STED} are the emission cross section, wavelength, and duration of the STED pulse, respectively.) As explained above, this expression incorporates the averaged near-field enhancement Γ_I experienced by the dye due to the presence of the metal NP, but is independent of the total decay rate k_{tot} and its enhancement factor Γ_k.[24]

In Figure 4C, the resolution with increasing STED power for both the NP and control experiments is shown, by plotting the measured fwhm's, averaged over several (≥25) nanoparticles per data point, as a function of the STED power P^{inc}_{STED}. The resolution obtained was as low as 75 nm, about 3.3 times better than the diffraction limit (as obtained by measuring both the control and NP sample under purely confocal conditions, i.e., without active STED beam). This is the main result of this paper, being the first demonstration of subdiffraction resolution in the context of STED nanoscopy with a hybrid plasmonic fluorescent label. Compared to the control sample, the NPs required less STED power to achieve the same resolution enhancement. By fitting the data to a standard depletion curve, we determined that the saturation power required for the NPs is reduced by ∼1/1.75 compared to the control. We repeated the measurements using shorter STED pulses (∼50 ps instead of ∼200 ps), in case the shortened lifetime within the NPs negatively influenced the STED efficiency. Whereas the shorter STED pulses depleted the fluorophores more efficiently overall, improving the spatial resolution down to ∼75 nm, the ratio of saturation powers remained identical to the measurements using the long pulses (Figure 4D). We estimated the saturation intensities I_{sat} of the samples to be about 8.1−10.0 MW/cm^2 for

DOI: 10.1021/acsphotonics.7b00833
ACS Photonics XXXX, XXX, XXX−XXX

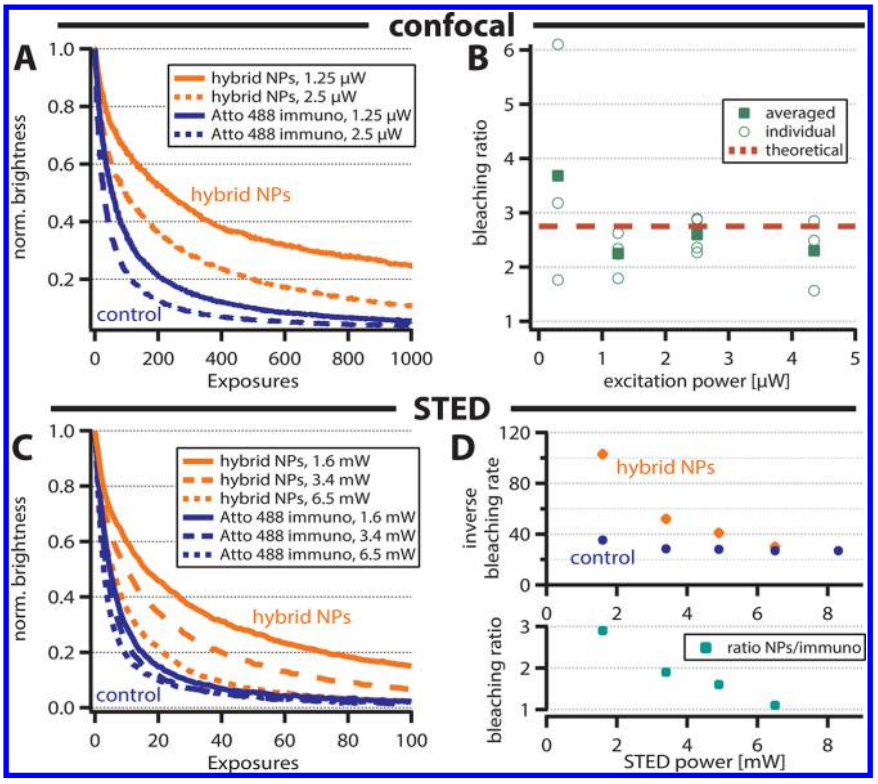

Figure 5. Bleaching behavior of hybrid NPs. (A) When illuminated with identical excitation powers (488 nm), the confocal signal recorded from the hybrid NPs (orange) bleaches away much more slowly than the control sample (blue). (B) The increased photostability of the NPs is mostly independent of the excitation power. (C) When imaging in STED mode (with both a 488 nm excitation and a 595 nm STED beam), the NPs (orange) again bleach more slowly than the control sample (blue). (D) The photostability is increased 3-fold at low STED powers, but as the STED intensity increases, the increased photostability of the NPs is counteracted, possibly by thermal destruction of the dye.

the control sample and 4.6−5.8 MW/cm^2 for the NPs. As compared to the theoretically predicted reduction in the required STED intensity of 1/1.18, the experimental result (1/1.75) is approximately 30% better. This discrepancy is explained by the differences in the emission cross section of the hybrid dye−NP label (0.1/0.14, see Figure 1C); however, other factors such as NP size dispersion, a nonuniform distribution of dye inside the shell, roughness of the surface of the metallic core, or the effect of the variation of the near-field enhancement Γ_I as the doughnut-shaped STED beam is scanned across the NP[27], may be playing a role as well.

Notably, the results were fully reversible and repeatable; no photodamage of the scanned region of interest or the neighboring regions was observed, nor any signs of boiling of the aqueous environment, such as bubbling, bleaching outside of the scanned areas, drifts, or movement of the NPs. In fact, we did not observe significant signs of melting or displacement of the NPs even at STED powers 2-fold higher (~45 mW) than used to determine the saturation intensities. Repeated imaging of the same region of interest revealed that even though at such high STED powers the fluorescence vanished quickly, the metal luminescence signals of the individual NPs remained fairly stable, i.e., bright, stationary, and unchanged in shape and size. Only at much higher powers (~70 mW) did we observe displacement and disappearance of the metal luminescence signals. The reason for limiting the STED powers to <25 mW was therefore not NP damage, but the ever-increasing metal luminescence signal (as mentioned earlier, see Figure 3A). Even with the more efficient gating due to the shorter STED pulses, at STED powers of >10 mW the metal luminescence was increasingly visible as a doughnut-shaped halo surrounding the fluorescence signal of the NPs. Furthermore, the high signal-to-noise ratio allowed a robust determination of the observed resolution improvement, contrary to the notably higher variation between individual NPs observed in the previous experimental demonstration with Au shells[27] or the more recent example with Au rods.[28] We were also able to utilize much higher STED intensities than before, possibly due to the lower metal volume, hence, yielding a higher threshold for damage from excess heating. Most importantly, unlike the initial demonstration of NP-STED where only a modest level of super-resolution was demonstrated,[27,28] here (NP-)STED enabled a substantial (>3-fold) improvement of resolution with respect to the diffraction limit, down to 75 nm.

Finally, we compared the photostability of the hybrid NPs and the control sample for both confocal and STED measurements. For this, we continuously imaged small areas of the sample (3 μm × 3 μm scan areas, pixel sizes of 100 nm (confocal) or 50 nm (STED), and pixel dwell-times between ~10 and 100 μs) until all or most of the fluorescence was bleached away, typically after 200−1000 exposures. The chosen image parameters were identical for both the NP and the control samples, and after each imaging series we checked for possible sample drift (no drift was detected). As before, we time-gated the detection signal. The bleaching was quantified by plotting the remaining signal brightness (total photons over the entire scan area) over number of exposures and fitting the resulting signal decay with a biexponential function; the inverse decay constants of the biexponential fits were dubbed the "bleaching rates", with lower bleaching rates signifying more

DOI: 10.1021/acsphotonics.7b00833
ACS Photonics XXXX, XXX, XXX−XXX

photostability. Such biexponential decay behavior has been observed before for various fluorescent dyes.[37,39] Both the fast and the slower bleaching rate showed near identical behavior for all the examined samples and imaging modalities. Thus, for simplicity, we will ignore the faster decay (with the higher variance) in favor of the slower one. As a measure of the improved photostability, we calculated the ratio of the inverse bleaching rates from the NP and the control sample, denoted as Γ_b.

Figure 5 shows the fluorescence decay using confocal and STED-enhanced imaging modalities. When imaging confocally, i.e., without the STED beam, the control samples bleached considerably faster than the dye protected within the hybrid NPs (Figure 5A). The bleaching ratio was found to be $\Gamma_b \approx 2-4$, seemingly irrespective of the excitation power (Figure 5B), in good agreement with the theoretically predicted value of 2.75 (red dashed). When performing STED imaging, we again observed slower bleaching of the hybrid NPs (Figure 5C); at low STED intensities, the bleaching rate of the signal from the hybrid labels was ~3 times lower than the bare dye. For higher STED power, however, the improved photostability of the hybrid labels decreased. Whereas the bleaching rate of the control sample remained roughly constant for increasing STED power, the bleaching of the hybrid NPs intensified, such that $\Gamma_b \rightarrow 1$ (Figure 5D). We ascribe this effect to damage occurring to the dye due to interaction between the STED beam and the gold cores (e.g., heating of the metal and its environment),[20] as this intense bleaching was also observed when illuminating the sample with only the STED beam, i.e., in the absence of the excitation beam.

DISCUSSION

The results detailed above provide a clear improvement with respect to previous demonstrations of NP-STED,[27,28] where only a modest super-resolution level was demonstrated (observed optical resolution was worse than 200 nm). Specifically, our demonstration of subdiffraction resolution of ~75 nm is the first time that hybrid plasmonic fluorescent nanoparticles are used to image well beyond the diffraction barrier of visible light in the context of STED microscopy. This is enabled by the 20-fold reduction of the label volume: from ~160 nm gold shells[27] to particles that are ~60 nm in diameter. Crucially, this means resolution levels better than those attainable by other approaches that offer limited subdiffraction resolution, including structured illumination microscopy[29] or other metal NP-based super-resolution techniques;[9,15] unlike the latter techniques, our approach can be applied to particles only a few nanometers in size. In addition, our results show nearly a ~2-fold reduction of STED intensity required for achieving the same resolution with the current generation of organic labels.

Our study also confirms, for the first time in the context of STED, the prediction regarding the reduction of bleaching ensuing from the use of the hybrid metal-fluorescent labels:[23] up to a 3-fold bleaching rate reduction was observed (in both confocal and STED modalities). This value is in good agreement with the theoretical prediction based on the theory presented previously,[20] thus showing that both additional bleaching reduction due to plasmonic-enhanced triplet lifetime shortening at the (resonant) STED wavelength[17] and bleaching due to multiphoton processes are probably of lesser importance, at least for the dye used in this study.

Note that the bleaching reduction (without using STED) reported here is qualitatively similar to previous observations based on either single molecules,[19] dye adsorbed onto a thin gold layer,[20] or dye contained within a polyelectrolyte multilayer film, onto which gold beads have been added.[18] Thus, we provide what seems to be the first demonstration of this concept using hybrid fluorescent labels, arguably, a more useful configuration. More importantly, however, in the confocal configuration our demonstration was obtained at substantially higher peak intensity, about 2 orders of magnitude higher due to the spatial and temporal focused nature of the illumination. Moreover, in the presence of a STED beam, the associated intensities were an additional 3−4 orders of magnitude higher. In the latter case, the depletion pulse, which enhances the decay from the excited level, modifies the quantitative description of the bleaching reduction[20] through the addition of an extra decay pathway. Unfortunately, the bleaching reduction persists only for relatively low STED powers, as for higher powers the interaction between the STED beam and the metal seems to cause dye destruction (possibly due to heating).[20] Yet, importantly, the bleaching rate is lower than in the bare-dye case in the whole range of intensities shown here.

Maybe the most important advance demonstrated in this study is that the imaging of the hybrid labels was performed in water (rather than in index matching oil, as was done so far[27,28]). This highlights the possibility of applying NP-STED to the study of biological samples. The applicability of NP-STED to live cell imaging, however, requires cell viability studies[45,46] to be carried out, in light of the transient temperature rise associated with the absorption in the metal. A discussion of ways to mitigate the (average) temperature rise is provided by Cortés et al.;[28] potentially the most efficient way to achieve that would be to employ stochastic spatial scanning (as already demonstrated[47]), yielding minimal average temperature rise.

Despite the important advances reported here, the performance improvement offered by the NP-STED hybrid labels used here is still limited. The major obstacle to achieving even better performance is NP miniaturization and, specifically, decreasing the metal volume. For one, this may enable higher near-field enhancement (hence, higher intensity reduction and maximal resolution) due to suppression of residual radiation damping.[1] Also, it would *further* limit the temperature rise due to absorption in the metal, as the latter is proportional to the physical cross section of the NP.[28,48,49] Importantly, a smaller metal nanoparticle will give rise to lower metal luminescence, thus facilitating the achievement of even better resolution (see discussion above) by enabling the use of even higher intensities and the extraction of brighter fluorescence signals. Thus (besides the obvious reduced damage to the biological system), NP size reduction would extend the benefit of bleaching reduction to higher intensities. In that regard, the shorter STED wavelength we employed (with respect to the more standard STED wavelength of 780 nm) is advantageous: it allows use of gold spheres, or slightly elongated gold rods, as the LPR of these particles is sufficiently close to the STED wavelength used in our system. Whereas we used particles with 20 nm Au cores, further miniaturization of the Au core and fluorescent shell is relatively easy to achieve, as was recently demonstrated.[28] We note, however, that the minimum total size of a good NP-STED label can practically not be much below 10−20 nm, since for fluorophore−metal separations of less than a few nanometers the apparent quantum yield of the fluorophore will be too

DOI: 10.1021/acsphotonics.7b00833
ACS Photonics XXXX, XXX, XXX−XXX

low due to fluorescence quenching. This could be compensated by the lower bleaching and by the possibility to increase the excitation intensity.[21] Thus, we expect that particles 2−3 times smaller than those used in the current studies are realistic and should yield superior imaging performance.

A second concern is obtaining a more significant field enhancement and thereby a higher reduction of the STED intensity. Further intensity reduction can be achieved by optimally matching the STED wavelength to the LPR band of the Au sphere.[23,24] This can be achieved by either shortening the STED wavelength or by using a STED dye with an emission line centered at even shorter wavelengths, such as AIE luminogen fluorophores.[50] Rod-shaped nanoparticles give rise to even better average intensity enhancement[28] and further control over the LPR wavelength. Furthermore, the ability of selective positioning of the dye with respect to the metal surface is continuously being advanced, such that NP-STED labels with improved performance, namely, higher field enhancement, lower quantum yield reduction, and moderate level of lifetime shortening, can be designed and synthesized. A step in this direction was already demonstrated[28] by replacing the thick dye-doped silica shell used here with fluorophores linked at a specific distance from the metal surface; they reported an 8-fold intensity enhancement, yet without improving the optical resolution beyond the previous demonstration. Applying a similar procedure for the Au nanospheres used here can lead to up to 3-fold higher field enhancement. Alternatively, in the context of fixed cell imaging, i.e., absent of living organisms, one could also employ Ag rods (considered toxic), for which the plasmonic performance far exceeds that of Au, thus enabling greater potential performance improvement in the NP-STED context.

Much higher intensity reduction (up to 50−100-fold) could be achieved with thin shells (instead of cores), such as those demonstrated previously;[51] in that work the cores were made of TiO_2, whereas for our purposes a core material that can be doped with fluorophores is desired, such as silica. Similarly, one could also employ quantum-dot cores, as STED has also recently been demonstrated with these emitters.[52] The somewhat shorter wavelength used in the current study also poses less stringent constraints on the thickness of gold shells. Synthesis of the necessary thin shells is still challenging, but within reach.

Overall, the excellent match of experimental results with the theoretical modeling gives us high confidence in our ability to reach the optimal performance predicted originally by Sivan et al.[23] Finally, the contrast between the very low damage threshold observed in previous demonstrations (with a gold shell[27] and a bare gold rod[28]) and its practical absence in the current study may imply that the silica shell serves also as a protection layer to the gold core. If so, the ideal NP-STED label design may rely on the smallest possible metal rods coated by a thin protecting layer that includes a thin layer of fluorophores/emitting semiconductor out of the quenching range.

Despite the limited improvement of performance demonstrated so far, there are three avenues where the existing hybrid labels could find immediate use. One is to use the useful characteristics of the hybrid NPs to bolster existing methods, which do not currently use nanoparticles. The reduced saturation intensities could benefit parallelized STED schemes,[53,54] where the lack of sufficient power can be a limiting factor in enabling the scan speed increase. Also, the reduced saturation intensities may also allow the application of STED to even thicker samples where the strong scattering reduces the incident STED intensities as one probes deeper into the tissue.

The second avenue entails using hybrid NPs as multifunctional labels to enable the combined use of very different imaging methods. Specifically, on one hand, operating in STED mode, one can benefit from the high spatial resolution levels at the emission wavelength; in the absence of a STED beam and for sufficiently intense excitation, one can benefit from the photothermal/photoacoustic response of the gold core[14,15,55] and the strong, spectrally narrow signal achievable above the nanolasing (also known as spasing) threshold enabled by the presence of feedback from the plasmonic cavity.[56] In the same modality, one can perform either bleaching-free imaging at enhanced resolution at the excitation wavelength via LPR-based structured illumination[10,57] using low intensities, quantitative phase contrast microscopy via the photothermal effect[16] using moderate intensities, or plasmonics-based saturated excitation (SAX) microscopy[8,9] using intense monochromatic illumination. One can also correlate the super-resolved STED signal with two-photon imaging[58] using moderate to high intensities. Ultimately, the hybrid labels studied here can help move toward correlated light electron imaging.[59]

The third avenue relies on enhancing the many existing biorelated applications of metal NPs (see ref 60) by adding a significant level of super-resolution imaging. These applications may include, for example, gene therapy treatments,[61] stimulation, monitoring and signaling in neurons,[62] and drug delivery.[11] One promising area is biodiagnostics[13] based on spherical nucleic acids,[63] which are quite similar to the NPs used in this study. The wide variety of associated applications includes protein targeting and selective colorimetric detection of polynucleotides,[64] scanometric DNA array detection,[65] and intracellular gene regulation,[66] to name just a few. These procedures, as well as any other that are currently imaged using confocal microscopy could benefit from the substantial improvement of the imaging resolution offered by NP-STED.

METHODS

Sample Preparation. The hybrid nanoparticles were diluted in pure water, then sonicated to ensure that no agglomeration occurred, and finally applied to coverslips coated with a thin poly-L-lysine layer (for increased stickiness of the surface). The coverslips were then briefly rinsed with pure water (to remove excess NPs and dye) and subsequently dried, before reimmersing them in a small drop of water and affixing the coverslip to the microscope slide. The particles had a density of approximately 5−10 beads per 1 μm^2, and only seldomly were there clusters of agglomerated beads. This way, we avoided tweezing effects and NP diffusion, which occurred previously. The control samples consisted of MeOH-fixated Vero cells, immunohistochemically stained with a primary anti-vimentin antibody (Sigma V6389, 1:100 dilution) and a secondary Atto-488 sheep/anti-mouse antibody (1:50 dilution) and mounted in Mowiol (with a refractive index of n = 1.45).

STED Nanoscope. All experiments were performed on a custom-built STED nanoscope[67] optimized for use with green fluorophores. For excitation, a 488 nm pulsed diode laser (PicoTA, Toptica Photonics, Graefelfing, Germany) was used with pulse lengths of ∼110 ps and typical laser powers between 1 and 10 μW in the back focal aperture of the objective lens. The STED beam was created using a Ti:sapphire laser (80 MHz; MaiTai, Spectra-Physics, Darmstadt, Germany), which

DOI: 10.1021/acsphotonics.7b00833
ACS Photonics XXXX, XXX, XXX−XXX

was frequency-shifted using an optical parametric oscillator (APE, Berlin, Germany) to a wavelength of 595 nm. The initially femtosecond pulses were prestretched using SF6 glass rods before being stretched further by either a short (25 m) or a long (110 m) polarization-maintaining glass fiber (OZ Optics, Ottawa, Canada), resulting in pulse widths of either approximately 50 or 200 ps, respectively. The typical power of the STED beam in the back focal aperture was between 1 and 25 mW. For our system, which employs a 80 MHz pulse repetition rate, a rough estimate shows that these power levels correspond to ∼17−425 MW/cm^2.

The beams were overlapped using custom-made dichroic mirrors and focused using a 1.3 NA glycerol immersion objective lens (63×, PL APO, CORR CS; Leica, Wetzlar, Germany). The fast scan axis was performed using resonant mirror scanning (15 kHz; SC-30, EOPC, Glendale, NY, USA) and the slow axis using a piezo stage (P-733; Physik-Instrumente, Karlsruhe, Germany). The fluorescence passed through a bandpass filter (535/60) and was recorded using a single-photon avalanche photo diode (SPAD, PDM series, Micro Photon Devices, Bolzano, Italy); images were recorded using the TTL output of the SPAD, whereas the fluorescence decay measurements used the fast NIM output with 35 ps time resolution and were counted using a time-correlated single-photon-counting module (SPC150N, Becker & Hickl, Berlin, Germany). A second detection window (450/60) could be used simultaneously for observing light outside of the Atto 488 fluorescence spectrum (i.e., metal luminescence).

Measurement Details. All STED images were recorded using time-gated detection, in order to distinguish fluorescence from any occurring metal luminescence. For this, the signal from the detector was time-gated electronically using a home-built circuit that separated the first 450 ps after onset of the excitation pulse from the rest of the signal, before relaying both signal components to the acquisition electronics, which were based on a custom field programmable gate array board. Nevertheless, when imaging the hybrid nanoparticles, we typically limited the applied STED power to <10 mW, to avoid saturating the detector, risk imaging artifacts due to residual metal luminescence, and/or damage to the NPs due to heating. This limited the achievable resolution to >100 nm (thus not sufficient to fully resolve the 60 nm hybrid nanoparticles), instead of the better than ∼50−70 nm resolution, which the STED nanoscope is capable of (when imaging control samples). At STED powers between ∼10 and 20 mW we still observed no NP damage or displacement; the metal luminescence, however, could not be gated away entirely, appearing as a doughnut-shaped halo surrounding the fluorescence signal of the NP. The lifetime of the dye under the various circumstances was determined by fitting the fluorescence decay using a routine implemented in Matlab (Mathworks, MA, USA), which iteratively reconvolved the instrument response function (IRF) with a mono- or biexponential decay function and then optimized the parameters. The IRF was acquired by reflecting the excitation or STED beam, respectively, off of a plane mirror sample and recorded using the same detection path as for the experiments. The IRF displayed a timing resolution of ∼110 ps fwhm for the 488 nm excitation beam and ∼200 ps fwhm for the 595 nm STED beam.

Theoretical Calculations and Modeling. To determine the electric field distribution for the core−shell geometry NPs, standard Mie theory[68] was used assuming an incident circularly polarized plane wave. Nominal values, provided by Nanocomposix Inc., of 18.8 and 20.5 nm were used for the inner core diameter and shell thickness, respectively. In all calculations, the properties of gold were taken from ref 69, while the refractive index of the silica coating and the aqueous host were taken as 1.4584 and 1.3324. The near-field enhancement Γ_I was determined by taking the ratio of the resulting intensity distribution as compared to that of a plane wave in a homogeneous Mowiol environment (n = 1.45), so as to match experimental controls. Volume averages were taken within the NP coating only. Results were verified using COMSOL 4.3a.

Position-dependent radiative Purcell factors, $F_r = P_r/P_0$, for dipole emitters oriented both radially and tangentially with respect to the core were calculated using a method based on accepted theory.[70] Specifically, the integrated power flow through a spherical surface in the far field (P_r) was compared to that of a free emitter embedded in Mowiol (P_0), for different emission wavelengths λ_{em}. The latter was found using the Larmour formula. Similarly, nonradiative Purcell factors ($F_{nr} = P_{nr}/P_0$) followed by calculating the power absorbed in the metal core, P_{nr}. The lifetime trace in Figure 2 was then calculated by considering the number of photons emitted by a dipole of given orientation $\mathbf{p}$ and position (neglecting photobleaching), which, as has been discussed previously,[33] is proportional to $N(\mathbf{r}, \hat{\mathbf{p}}, t) \approx |\hat{\mathbf{p}}\cdot\mathbf{E}|F_r \exp[-(F_r + F_{nr} + \eta_0^{-1} - 1)t/\tau_0]$, where $\eta_0 = 0.8$ (τ_0) is the quantum yield (lifetime) of a free emitter, caret notation denotes a unit vector, and $\mathbf{E}$ is the electric field at the position of the dipole upon illumination of the NP with a plane wave. We note that although the importance of the orientation of the dye molecule was known,[18] in many earlier theoretical treatments a fixed emitter orientation was considered, e.g., due to preferential adsorption.[20] In contrast, since our system comprises dye molecules doped in a silica coating, we allowed for a random distribution of emitter orientations, in turn requiring a further averaging step to be introduced in our modeling. Specifically, we assumed that the dye molecules were oriented randomly over the full 4π solid angle Ω, whereby the total collected signal N_T was found by integrating over the volume of the shell and averaging over the orientation. Each spectral component was further weighted according to the Atto 488 emission spectrum $w(\lambda_{em})$ such that the fluorescence intensity scales as

$$I(t) \approx \frac{1}{4\pi}\int_0^\infty \int_\Omega \int_V w(\lambda_{em})\, N_T(\mathbf{r}, \hat{\mathbf{p}}, t, \lambda_{em})\, d\mathbf{r}\, d\hat{\mathbf{p}}\, d\lambda_{em} \quad (1)$$

Note that the F_r factor present in N_T accounts for modification of the spectral profile of the isolated fluorophore.[71,72] Finally, the resulting fluorescence trace was convolved with the measurement IRF. We note there were no free parameters in our calculation. The effective lifetime was extracted using a monoexponential fit. Calculations were repeated for inner core diameters and shell thicknesses of 18.8 ± 1.9 nm and 20.5 ± 1.1 nm to estimate the effects of size dispersion as quoted in the main text.

Since the lifetime of differently oriented and positioned emitters within the NP is modified to varying extents, the relative competition between radiative decay, nonradiative decay, and photobleaching also varies. The effective bleaching rate of a given emitter can be determined as in ref 20; however, the resultant bleaching curves (cf. Figure 5) will, similarly to the lifetime traces, be formed of the superposition of multiple-

DOI: 10.1021/acsphotonics.7b00833
ACS Photonics XXXX, XXX, XXX−XXX

exponential curves. Using a normalized time coordinate, the decay constants in the exponents are given by $\alpha\Gamma_I/[F_r + F_{nr} + \eta_0^{-1} - 1]$, where $\alpha = |\hat{\mathbf{p}}\cdot\hat{\mathbf{E}}|^2/|\hat{\mathbf{p}}\cdot\hat{\mathbf{E}}_0|^2$ describes the relative polarization rotation from the NP. The relative weighting of the individual bleaching curves depends on the local near-field intensity enhancement Γ_I and the ratio $F_r/(F_r + F_{nr})$.[20] Volume, orientation, and wavelength averages were taken similarly to eq 1. To parallel the experimental treatment, monoexponential fits were used to determine effective decay rates and hence the theoretical bleaching ratio Γ_b.

AUTHOR INFORMATION

Corresponding Author

*E-mail: sivanyon@bgu.ac.il.

ORCID

Matthew R. Foreman: 0000-0001-5864-9636

Stefan W. Hell: 0000-0002-9638-5077

Yonatan Sivan: 0000-0003-4361-4179

Present Address

[‖]Max Planck Florida Insitute for Neuroscience, Jupiter, Florida 33458, United States.

Notes

The authors declare no competing financial interest.

ACKNOWLEDGMENTS

We would like to thank T. Klar, K. Matsuzaki, S. Sahl, and H. Sinclair for helpful discussions. M.R.F. is funded by a Royal Society University Research Fellowship. Y.S. acknowledges support from the People Programme (Marie Curie Actions) of the EU's Seventh Framework Programme (FP7/2007-2013) under REA grant agreement no. 333790, the Alumni Program of the Royal Society International Newton Fellowship Program, and the Israeli National Nanotechnology Initiative.

REFERENCES

(1) Giannini, V.; Fernández-Domínguez, A. I.; Heck, S. C.; Maier, S. A. Plasmonic nanoantennas: fundamentals and their use in controlling the radiative properties of nanoemitters. *Chem. Rev.* **2011**, *111*, 3888.

(2) Atwater, H. A.; Polman, A. Plasmonics for improved photovoltaic devices. *Nat. Mater.* **2010**, *9*, 205−213.

(3) Neumann, O.; Urban, A. S.; Day, J.; Lal, S.; Nordlander, P.; Halas, N. J. Solar Vapor Generation Enabled by Nanoparticles. *ACS Nano* **2013**, *7*, 42−49.

(4) Fang, Z.; Zhen, Y. R.; Neumann, O.; Polman, A.; de Abajo, F. J. G.; Nordlander, P.; Halas, N. J. Evolution of Light-Induced Vapor Generation at a Liquid-Immersed Metallic Nanoparticle. *Nano Lett.* **2013**, *1736−1742*, 13.

(5) Baaske, M. D.; Vollmer, F. Optical observation of single atomic ions interacting with plasmonic nanorods in aqueous solution. *Nat. Photonics* **2016**, *10*, 733−739.

(6) Le Ru, E. C.; Etchegoin, P. G. *Principles of Surface-Enhanced Raman Spectroscopy and Related Plasmonic Effects*; Elsevier: Amsterdam, 2009.

(7) Baffou, G.; Quidant, R. Nanoplasmonics for chemistry. *Chem. Soc. Rev.* **2014**, *43*, 3898.

(8) Chu, S.-W.; Wu, H.-Y.; Huang, Y.-T.; Su, T.-Y.; Lee, H.; Yonemaru, Y.; Yamanaka, M.; Oketani, R.; Kawata, S.; Fujita, K. Saturation and Reverse Saturation of Scattering in a Single Plasmonic Nanoparticle. *ACS Photonics* **2013**, *1*, 32−37.

(9) Chu, S.-W.; Su, T.-Y.; Oketani, R.; Huang, Y.-T.; Wu, H.-Y.; Yonemaru, Y.; Yamanaka, M.; Lee, H.; Zhuo, G.-Y.; Lee, M.-Y.; Kawata, S.; Fujita, K. Measurement of a Saturated Emission of Optical Radiation from Gold Nanoparticles: Application to an Ultrahigh Resolution Microscope. *Phys. Rev. Lett.* **2014**, *112*, 017402.

(10) Ponsetto, J. L.; Wei, F.; Liu, Z. Localized plasmon assisted structured illumination microscopy for wide-field high-speed dispersion- independent super resolution imaging. *Nanoscale* **2014**, *6*, 5807−5812.

(11) Xia, X.; Xia, Y. Gold nanocages as multifunctional materials for nanomedicine. *Front. Phys.* **2014**, *9*, 378−384.

(12) Hirsch, L. R.; Stafford, R. J.; Bankson, J. A.; Sershen, S. R.; Rivera, B.; Price, R. E.; Hazle, J. D.; Halas, N. J.; West, J. L. Nanoshell-mediated near-infrared thermal therapy of tumors under magnetic resonance guidance. *Proc. Natl. Acad. Sci. U. S. A.* **2003**, *100*, 13549−13554.

(13) Rosi, N. L.; Mirkin, C. A. Nanostructures in Biodiagnostics. *Chem. Rev.* **2005**, *105*, 1547.

(14) Zharov, V. P. Ultrasharp nonlinear photothermal and photoacoustic resonances and holes beyond the spectral limit. *Nat. Photonics* **2011**, *5*, 110−116.

(15) Danielli, A.; Maslov, K.; Uribe, A. G.; Winkler, A.; Li, C.; Wang, L.; Chen, Y.; Dorn, G.; Wang, L. V. Label-free photoacoustic nanoscopy. *J. Biomed. Opt.* **2014**, *19*, 086006.

(16) Blum, O.; Shaked, N. Prediction of photothermal phase signatures from arbitrary plasmonic nanoparticles and experimental verification. *Light: Sci. Appl.* **2015**, *4*, 322.

(17) Kéna-Cohen, S.; Wiener, A.; Sivan, Y.; Stavrinou, P. N.; Bradley, D. D. C.; Horsefield, A.; Maier, S. A. Plasmonic sinks for the selective removal of long-lived states. *ACS Nano* **2011**, *5*, 9958−65.

(18) Cang, H.; Liu, Y.; Wang, Y.; Yin, X.; Zhang, X. Giant Suppression of Photobleaching for Single Molecule Detection via the Purcell Effect. *Nano Lett.* **2013**, *13*, 5949−5953.

(19) Pellegrotti, J. V.; Acuna, G. P.; Puchkova, A.; Holzmeister, P.; Gietl, A.; Lalkens, B.; Stefani, F. D.; Tinnefeld, P. Controlled reduction of photobleaching in DNA origami-gold nanoparticle hybrids. *Nano Lett.* **2014**, *14*, 2831−2836.

(20) Galloway, C. M.; Artur, C.; Grand, J.; Le Ru, E. Photobleaching of fluorophores on the surface of nanoantennas. *J. Phys. Chem. C* **2014**, *118*, 28820−28830.

(21) Wientjes, E.; Renger, J.; Cogdell, R.; van Hulst, N. F. Pushing the Photon Limit: Nanoantennas Increase Maximal Photon Stream and Total Photon Number. *J. Phys. Chem. Lett.* **2016**, *7*, 1604−1609.

(22) Hell, S. W. Nobel Lecture: Nanoscopy with freely propagating light. *Rev. Mod. Phys.* **2015**, *87*, 1169.

(23) Sivan, Y.; Sonnefraud, Y.; Kéna-Cohen, S.; Pendry, J. B.; Maier, S. A. Nanoparticle-assisted stimulated emission depletion nanoscopy. *ACS Nano* **2012**, *6*, 5291−5296.

(24) Sivan, Y. Performance improvement in nanoparticle-assisted stimulated emission depletion nanoscopy. *Appl. Phys. Lett.* **2012**, *101*, 021111.

(25) Sivan, Y.; Sonnefraud, Y. *Plasmonics and Super Resolution Imaging*; Liu, Z., Ed.; PAN Stanford, to appear, 2017.

(26) Balzarotti, F.; Stefani, F. Plasmonics Meets Far-Field Optical Nanoscopy. *ACS Nano* **2012**, *6*, 4580.

(27) Sonnefraud, Y.; Sinclair, H. G.; Sivan, Y.; Foreman, M. R.; Dunsby, C.; Neil, M. A. A.; French, P. M.; Maier, S. A. Experimental Proof of Concept of Nanoparticle-Assisted STED. *Nano Lett.* **2014**, *14*, 4449−4453.

(28) Cortés, E.; Huidobro, P. A.; Sinclair, H. G.; Guldbrand, S.; Peveler, W. J.; Davies, T.; Parrinello, S.; Görlitz, F.; Dunsby, C.; Neil, M. A. A.; Sivan, Y.; Parkin, I. P.; French, P. M.; Maier, S. A. Plasmonic nanoprobes for stimulated emission depletion microscopy. *ACS Nano* **2016**, *10*, 10454−10461.

(29) Gustafsson, M. Surpassing the lateral resolution limit by a factor of two using structured illumination microscopy. *J. Microsc.* **2000**, *198*, 82−87.

(30) Raab, M.; Vietz, C.; Stefani, F. D.; Acuna, G. P.; Tinnefeld, P. Shifting molecular localization by plasmonic coupling in a single-molecule mirage. *Nat. Commun.* **2017**, *8*, 13966.

(31) Foreman, M. R.; Sivan, Y.; Maier, S. A.; Török, P. Independence of plasmonic near-field enhancements to illumination beam profile. *Phys. Rev. B: Condens. Matter Mater. Phys.* **2012**, *86*, 155441.

DOI: 10.1021/acsphotonics.7b00833
ACS Photonics XXXX, XXX, XXX−XXX

(32) Lakowicz, J. *Principles of Fluorescence Spectroscopy*, 3rd ed.; Springer: New York, 2006.
(33) Akselrod, G. M.; Argyropoulos, C.; Hoang, T. B.; Ciraci, C.; Fang, C.; Huang, J.; Smith, D. R.; Mikkelsen, M. H. Probing the mechanisms of large Purcell enhancement in plasmonic nanoantennas. *Nat. Photonics* **2014**, *8*, 835.
(34) Bakker, R. M.; Drachev, V. P.; Liu, Z.; Yuan, H. K.; Pedersen, R. H.; Boltasseva, A.; Chen, J.; Irudayaraj, J.; Kildishev, A. V.; Shalaev, V. M. Nanoantenna array-induced fluorescence enhancement and reduced lifetimes. *New J. Phys.* **2008**, *10*, 125022.
(35) Moffitt, J. R.; Osseforth, C.; Michaelis, J. Time-gating improves the spatial resolution of STED microscopy. *Opt. Express* **2011**, *19*, 4242−4254.
(36) Vicidomini, G.; Moneron, G.; Han, K. Y.; Westphal, V.; Ta, H.; Reuss, M.; Engelhardt, J.; Eggeling, C.; Hell, S. W. Sharper low-power STED nanoscopy by time-gating. *Nat. Methods* **2011**, *8*, 571−3.
(37) Eggeling, C.; Widengren, J.; Rigler, R.; Seidel, C. A. M. Photobleaching of fluorescent dyes under conditions used for single-molecule detection: Evidence of two-step photolysis. *Anal. Chem.* **1998**, *70*, 2651−59.
(38) Bout, D. A. V.; Deschenes, L. A. Single molecule photobleaching: increasing photon yield and survival time through suppression of two-step photolysis. *Chem. Phys. Lett.* **2002**, *365*, 387−95.
(39) Eggeling, C.; Volkmer, A.; Seidel, C. A. M. Molecular Photobleaching Kinetics of Rhodamine 6G by One- and Two-Photon Induced Confocal Fluorescence Microscopy. *ChemPhysChem* **2005**, *6*, 791−804.
(40) Enderlein, J. Theoretical study of single molecule fluorescence in a metallic nanocavity. *Appl. Phys. Lett.* **2002**, *80*, 315−317.
(41) Enderlein, J. Spectral properties of a fluorescing molecule within a spherical metallic nanocavity. *Phys. Chem. Chem. Phys.* **2002**, *4*, 2780−6.
(42) Mooradian, A. Photoluminescence of metals. *Phys. Rev. Lett.* **1969**, *22*, 185.
(43) Park, J.; Estrada, A.; Sharp, K.; Sang, K.; Schwartz, J. A.; Smith, D. K.; Coleman, C.; Payne, J. D.; Korgel, B. A.; Dunn, A. K.; Tunnell, J. W. Two-photon-induced photoluminescence imaging of tumors using near-infrared excited gold nanoshells. *Opt. Express* **2008**, *16*, 1590.
(44) Leutenegger, M.; Eggeling, C.; Hell, S. W. Analytical description of STED microscopy performance. *Opt. Express* **2010**, *18*, 26417−26429.
(45) Dewhirst, M. W.; Viglianti, B. L.; Lora-Michiels, M.; Hanson, M.; Hoopes, P. J. Basic principles of thermal dosimetry and thermal thresholds for tissue damage from hyperthermia. *Int. J. Hyperthermia* **2003**, *19*, 267−294.
(46) Wäldchen, S.; Lehmann, J.; Klein, T.; van de Linde, S.; Sauer, M. Light-induced cell damage in live-cell super-resolution microscopy. *Sci. Rep.* **2015**, *5*, 15348.
(47) Schneider, J.; Zahn, J.; Maglione, M.; Sigrist, S. J.; Marquard, J.; Chojnacki, J.; Kräusslich, H.-G.; Sahl, S. J.; Engelhardt, J.; Hell, S. W. Ultrafast, temporally stochastic STED nanoscopy of millisecond dynamics. *Nat. Methods* **2015**, *12*, 827.
(48) Baffou, G.; Quidant, R. Thermo-plasmonics: using metallic nanostructures as nano-sources of heat. *Laser Photonics Rev.* **2013**, *7*, 171−187.
(49) Sivan, Y.; Chu, S.-W. Nonlinear plasmonics at high temperatures. *Nanophotonics* **2017**, *6*, 317−328.
(50) Yu, J.; Sun, X.; Cai, F.; Zhu, Z.; Qin, A.; Qian, J.; Tang, B.; He, S. Low photobleaching and high emission depletion efficiency: the potential of AIE luminogen as fluorescent probe for STED microscopy. *Opt. Lett.* **2015**, *40*, 2313−16.
(51) Dang, X.; Qi, J.; Klug, M. T.; Chen, P.-Y.; Yun, D. S.; Fang, N. X.; Hammond, P. T.; Belcher, A. M. Tunable Localized Surface Plasmon-Enabled Broadband Light-Harvesting Enhancement for High-Efficiency Panchromatic Dye-Sensitized Solar Cells. *Nano Lett.* **2013**, *13*, 637−642.
(52) Hanne, J.; Falk, H. J.; Görlitz, F.; Hoyer, P.; Engelhardt, J.; Sahl, S. J.; Hell, S. W. STED nanoscopy with fluorescent quantum dots. *Nat. Commun.* **2015**, *6*, 7127.
(53) Yang, B. B.; Przybilla, F.; Mestre, M.; Trebbia, J. B.; Lounis, B. Large parallelization of STED nanoscopy using optical lattices. *Opt. Express* **2014**, *22*, 5581−5589.
(54) Bergermann, F.; Alber, L.; Sahl, S. J.; Engelhardt, J.; Hell, S. W. 2000-fold parallelized dual-color STED fluorescence nanoscopy. *Opt. Express* **2015**, *23*, 211−223.
(55) Zharov, V. P.; Lapotko, D. O. Photothermal imaging of nanoparticles and cells. *IEEE J. Sel. Top. Quantum Electron.* **2005**, *11*, 733−751.
(56) Galanzha, E. I.; Weingold, R.; Nedosekin, D. A.; Sarimollaoglu, M.; Kuchyanov, A. S.; Parkhomenko, R. G.; Plekhanov, A. I.; Stockman, M. I.; Zharov, V. P. Spaser as Novel Versatile Biomedical Tool. *arXiv:1501.00342 [cond-mat.mes-hall]*, 2015,.
(57) Fernández-Domínguez, A. I.; Liu, Z.; Pendry, J. B. Coherent Four-Fold Super-Resolution Imaging with Composite Photonic-Plasmonic Structured Illumination. *ACS Photonics* **2015**, *2*, 341−348.
(58) Durr, N. J.; Larson, T.; Smith, D. K.; Korgel, B.; Sokolov, K.; Ben-Yakar, A. Two-Photon Luminescence Imaging of Cancer Cells Using Molecularly Targeted Gold Nanorods. *Nano Lett.* **2007**, *4*, 941−945.
(59) Perkovic, M.; Kunz, M.; Endesfelder, U.; Bunse, S.; Wigge, C.; Yu, Z.; Hodirnau, V. V.; Scheffer, M. P.; Seybert, A.; Malkusch, S.; Schuman, E. M.; Heilemann, M.; Frangakis, A. S. Correlative Light- and Electron Microscopy with chemical tags. *J. Struct. Biol.* **2014**, *186*, 205−213.
(60) Webb, J. A.; Bardhan, R. Emerging advances in nanomedicine with engineered gold nanostructures. *Nanoscale* **2014**, *6*, 941−945.
(61) Lachaine, R.; Boutopoulos, C.; Lajoie, P.-Y.; Boulais, E.; Meunier, M. Rational Design of Plasmonic Nanoparticles for Enhanced Cavitation and Cell Perforation. *Nano Lett.* **2016**, *16*, 3187−3194.
(62) Lavoie-Cardinal, F.; Salesse, C.; Bergeron, E.; Meunier, M.; Koninck, P. D. Gold nanoparticle-assisted all optical localized stimulation and monitoring of Ca2+ signaling in neurons. *Sci. Rep.* **2016**, *6*, 20619.
(63) Mirkin, C. A. A DNA-based method for rationally assembling nanoparticles into macroscopic materials. *Nature* **1996**, *382*, 607−609.
(64) Elghanian, R.; Storhoff, J. J.; Mucic, R. C.; Letsinger, R. L.; Mirkin, C. A. Selective Colorimetric Detection of Polynucleotides Based on the Distance-Dependent Optical Properties of Gold Nanoparticles. *Science* **1997**, *277*, 1078.
(65) Taton, T. A.; Mirkin, C. A.; Letsinger, R. L. Scanometric DNA Array Detection with Nanoparticle Probes. *Science* **2000**, *289*, 1757.
(66) Young, K. L.; Scott, A. W.; Hao, L.; Mirkin, S. E.; Liu, G.; Mirkin, C. A. Hollow Spherical Nucleic Acids for Intracellular Gene Regulation Based upon Biocompatible Silica Shells. *Nano Lett.* **2012**, *12*, 3867.
(67) Urban, N. T.; Willig, K. I.; Hell, S. W.; Nägerl, U. V. STED Nanoscopy of Actin Dynamics in Synapses Deep Inside Living Brain Slices. *Biophys. J.* **2011**, *101*, 1277−1284.
(68) Aden, A. L.; Kerker, M. Scattering of Electromagnetic Waves from Two Concentric Spheres. *J. Appl. Phys.* **1951**, *22*, 1242−1246.
(69) Palik, E. *Handbook of Optical Constants of Solids*, 2nd ed.; Academic Press, 1998.
(70) Moroz, A. A recursive transfer-matrix solution for a dipole radiating inside and outside a stratified sphere. *Ann. Phys.* **2005**, *315*, 352−418.
(71) Le Ru, E. C.; Etchegoin, P. G.; Grand, J.; Félidj, N.; Aubard, J.; Lévi, G. Mechanisms of Spectral Profile Modification in Surface-Enhanced Fluorescence. *J. Phys. Chem. C* **2007**, *111*, 16076−16079.
(72) Ringler, M.; Schwemer, A.; Wunderlich, M.; Nichtl, A.; Kürzinger, K.; Klar, T. A.; Feldmann, J. Shaping Emission Spectra of Fluorescent Molecules with Single Plasmonic Nanoresonators. *Phys. Rev. Lett.* **2008**, *100*, 203002.

DOI: 10.1021/acsphotonics.7b00833
ACS Photonics XXXX, XXX, XXX−XXX